Check for updates

Highly emissive dibenzofuranfluorophores with aggregation-induced emission for bioimaging in HeLa cell lines

Nikita Kush Durgi[ab] and Prasad Pralhad Pujar [ID] *[ab]

Dibenzo[*b,d*]furans, structural analogs of furan, represent an emerging class of promising molecules whose solid-state emission properties remain largely unexplored. The aim of the present work is to design and synthesize new dibenzo[*b,d*]furan-based organic fluorophores for bioimaging applications. The synthesis involved a single-step Schiff base reaction of 4-(dibenzo[*b,d*]furan-4-yl)aniline with two different *ortho*-hydroxy aldehydes, furnishing **DBF1** and **DBF2** in high yields. Both fluorophores **DBF1** and **DBF2** exhibited high fluorescence in their solid and aggregated states. The photophysical properties in solution, solid, and aggregated states were investigated using absorbance and emission spectroscopy. The aggregation process was confirmed by the particle size analysis using dynamic light scattering (DLS). The cytotoxicity of the molecules was investigated against HeLa cell lines by the standard MTT assay. **DBF1** and **DBF2** demonstrated exceptional photoluminescence with quantum yields reaching up to 17.89% and 2.26% respectively, highlighting their potential as excellent materials for imaging applications. Both **DBF1** and **DBF2** exhibited significant toxicity towards HeLa cells with IC_{50} values of 42.08 μg ml^{-1} and 39.74 μg ml^{-1}, respectively, showcasing notable anti-proliferative activity against HeLa cells. Both fluorophores exhibited excellent emission in HeLa cells with mean relative fluorescence intensities of 1.008 ± 0.77 a.u. and 1.44 ± 0.65 a.u. for **DBF1** and **DBF2**, respectively. Thus, this work presents the lesser explored dibenzo[*b,d*]furan-based organic fluorophores for bioimaging applications with potential inhibitory activity against HeLa cells.

aDepartment of Chemistry, Christ University, Hosur Road, Bangalore, Karnataka 560029, India

bCentre for Renewable Energy and Environmental Sustainability, Christ University, Bangalore 560029, India. E-mail: prasad.pujar@christuniversity.in

1 Introduction

Fluorescence imaging is a powerful tool to detect and monitor substances and biochemical processes within a biological environment due to its high selectivity, sensitivity, and non-invasive method of operation.[1–4] An enormous amount of effort has been put into developing non-toxic, highly sensitive, and selective fluorophores for compelling imaging of biological systems.[5,6] Due to the non-fluorescent nature of biological systems, the present fluorescence imaging techniques mainly utilize fluorescent dyes and nanoparticles to visualize the biological systems.[7–9] Although organic fluorophores are the most versatile fluorescent materials because of their easy cell penetration, high sensitivity, and structural flexibility, there are many shortcomings that limit their practical applications.[10,11] The major drawback of these organic fluorophores is that they are poorly soluble in water and undergo aggregation-caused quenching (ACQ) in aqueous media, leading to low fluorescence intensity.[12] Additionally, these fluorophores have very low target-to-background intensity ratios and are emissive even in the non-target areas, affecting their sensitivity and selectivity.[13] Therefore, developing new, non-toxic, solid-state AIE-active fluorophores with promising applications in bioimaging, biosensing, and fluorescence image-aided surgeries is very crucial.[14,15]

Excited state intramolecular proton transfer (ESIPT) is a rapid phototautomerization between a proton donor (–OH, –NH_2, *etc.*) and a proton acceptor (–C=O, –N=C, *etc.*) present in the immediate vicinity.[16] ESIPT-active luminophores have attracted a lot of attention recently due to their high fluorescence quantum yield and large Stokes shift without self-absorption.[17–19] A significant amount of ESIPT-active compounds have been reported for various applications such as laser dyes, photo stabilisers, fluorescent materials, OLEDs, biosensors, and bioimaging, *etc.*[20–24] By leveraging high fluorescence quantum yields and large Stokes shifts, of ESIPT based molecules and combining them with aggregation induced emission (AIE) property has been the most effective strategy used by many researchers to achieve highly emissive solid-state fluorophores for diverse applications including biosensing and bioimaging.[25–27]

Furan and benzofuran scaffolds are well-known for their biological applications.[28–30] However, dibenzo[*b,d*]furan is the
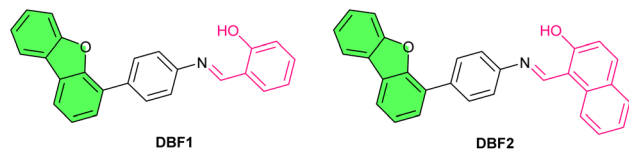
Fig. 1 Molecular structures of fluorophores **DBF1** and **DBF2** synthesized in this work.

lesser explored heterocyclic moiety, particularly for fluorescence applications. To the best of our knowledge, dibenzo[b,d]furan-based molecules have not been explored for their fluorescence imaging applications so far. Considering the high conjugation of benzofuran-based scaffolds, herein we have designed two dibenzo[b,d]furan-based molecules, **DBF1** and **DBF2** (Fig. 1), having solid-state emissive fluorophores as a result of a synergic effect of ESIPT and AIE/AIEE to realize their applications in bioimaging in HeLa cell lines. These fluorophores exhibited high fluorescence emission in HeLa cell lines. The cytotoxic effects of these fluorophores against HeLa cells have been discussed in this study. The present study evaluates the

bioimaging applications of meticulously tailored dibenzo[b,d] furan-based fluorophores against HeLa cell lines. Photophysical and AIE studies were conducted to support the emission mechanism in solid and aggregated states of fluorophores.

2 Results and discussion

2.1 Photophysical properties

The photophysical properties of the synthesized molecules **DBF1** and **DBF2** were investigated using absorbance and emission spectroscopy. **DBF1** showed a yellow fluorescence, and **DBF2** showed green fluorescence under UV 365 nm illumination in their solid state. The solid-state excitation and emission spectra of **DBF1** and **DBF2** are shown in Fig. 2. The emission spectra of **DBF1** showed a single emission band with a λ_{em} maximum at 549 nm, and **DBF2** showed a dual emission band with emission maxima at 514 nm and 617 nm. Owing to the typical structural features of **DBF1**, a Schiff base with a phenolic hydroxy group in the *ortho* position (salicylaldehyde-based Schiff base) is perfect for ESIPT behavior.[26] In the case of
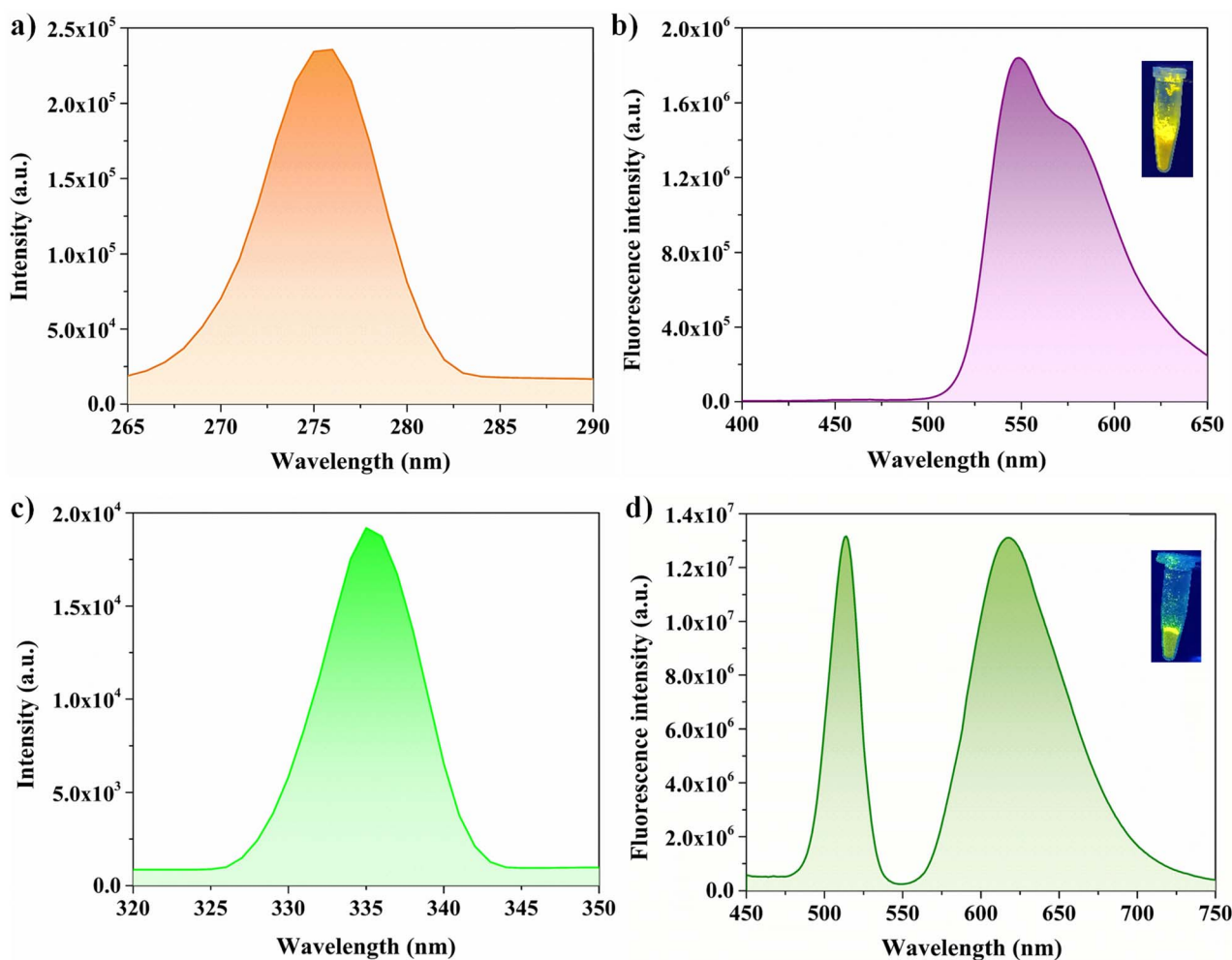

Fig. 2 (a) Excitation and (b) emission spectra of **DBF1** (excitation wavelength = 345 nm). (c) Excitation spectra and (d) emission spectra of **DBF2** (excitation wavelength = 324 nm).

DBF2, a dual emission in the solid state gives irrefutable evidence for the presence of ESIPT phenomena.[31]

The fluorescent molecules are sensitive to environmental changes, especially those based on the ESIPT mechanism. Therefore, we investigated the effect of solvent polarity changes (solvatochromic properties) on the emission properties of the molecules. The solvatochromic properties of **DBF1** and **DBF2** (concentration used = 30 μM) were studied using absorption and emission spectroscopy. The absorbance and emission spectra of the synthesized molecules were recorded in seven different solvents of varying polarities, including acetonitrile, ethyl acetate, ethanol, hexane, tetrahydrofuran, DMSO, and toluene. The absorbance spectra of **DBF1** and **DBF2** in varying solvent polarities can be found in the SI (Fig. S9). For both **DBF1** and **DBF2**, the absorbance spectrum showed few variations in the absorbance with varying polarities. However, in the case of **DBF2**, dual nature peaks were observed in highly polar solvents such as EtOH, acetonitrile, and DMSO. This shows that both keto and enol forms coexist in polar solvents, substantiating ESIPT involvement. New broad peaks were also observed in these polar solvents in the range of 450–500 nm in the absorbance spectrum, which was attributed to the phenoxide ion generated *via* deprotonation induced by intermolecular hydrogen bonding between the phenolic hydroxyl group and solvent molecules, as reported earlier.[32,33]

As shown in Fig. 3, the emission of **DBF1** and **DBF2** was found to be low in the solution state compared to the solid-state emission (Fig. 2). For **DBF1** (Fig. 3a), a red shift in the emission maxima was observed for all the solvents as the polarity increased. With the increase in the polarity of the solvents, the Stokes shift also increased (Tables S1 and S2), showing a positive solvatochromic effect. For **DBF2** (Fig. 3b), even though a similar trend to **DBF1** was observed, a slight variation was found, wherein the emission maxima of acetonitrile were more red-shifted than ethanol, contrary to the observation made in the case of **DBF1**. However, Stokes shift showed a gradual increase with the increase in the solvent polarity, the same as in the case of **DBF1**. Typically, these significant shifts in Stokes shifts (Tables S1 and S2) can effectively avoid the self-absorption of fluorophores, which is advantageous for their applications in biological imaging. Moreover, this increase in Stokes shift advocates for the ESIPT mechanism to be involved in the highly emissive nature of the aggregated state.

2.2 Aggregation-induced emission or aggregation-induced enhanced emission (AIE/AIEE)

To investigate the photophysical properties of **DBF1** and **DBF2** in an aggregated state, THF: water fractions (concentration used = 30 μM) were used. The absorbance and emission spectra were recorded for both compounds in THF with varying water fractions. For both compounds, long tails were observed in the absorbance spectra (Fig. S10), resulting from Mie scattering, indicating the formation of aggregates.[34–36] **DBF1**, with an increase in the water fractions, showed a red shift from 348 nm for 0% water fraction to 359.5 nm for 90% water fraction in THF solvent. Whereas, for **DBF2**, a dual emission nature was found, which was attributed to the absorbance from the enol form of **DBF2** at 324 nm in pure THF (0% water fraction) and the other emerging at a longer wavelength, possibly due to the keto form at 386 nm.

The emission profiles of both compounds were evaluated in the aggregated state by taking the solution of the compounds in THF with varying water fractions (0–90% water fractions). An increase in the water fractions showed increased emission intensity for both compounds (Fig. 4). For **DBF1**, the emission intensity gradually increased with an increase in water fractions up to 70% water fraction and then decreased. This decrease in emission intensity was due to the precipitation of the aggregates (agglomeration) of the molecules as a result of the scattering of light. As shown in Fig. 4a, the emission intensity increases and reaches its maximum at 70% water fraction. This enhanced emission at higher water fractions confirms the
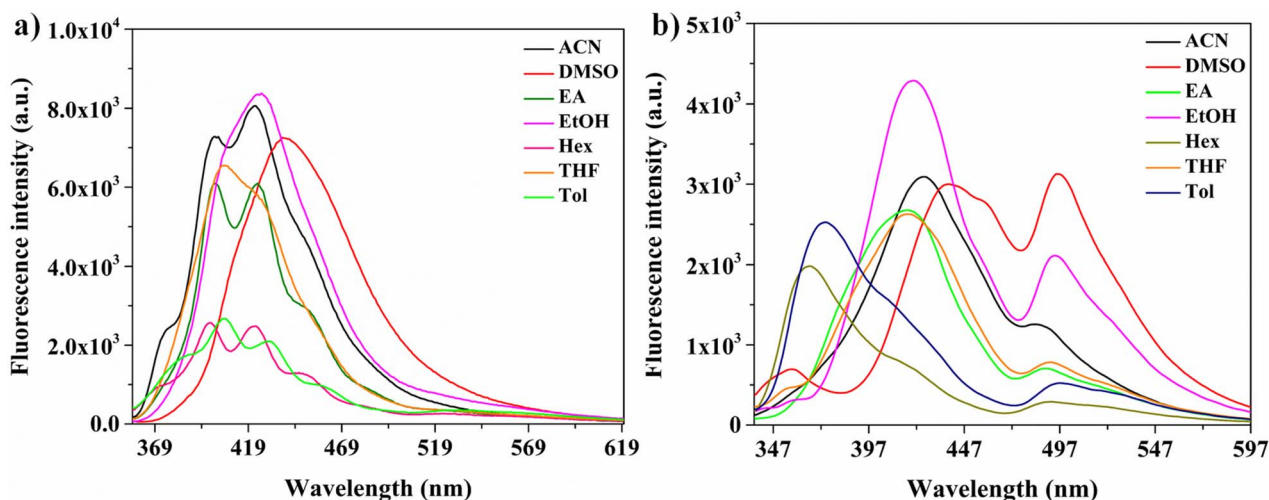

Fig. 3 Emission spectra of (a) **DBF1** and (b) **DBF2** with different polarity solvents (excitation wavelength 345 nm) for **DBF1** and 324 nm for **DBF2** [concentration = 30 μM].
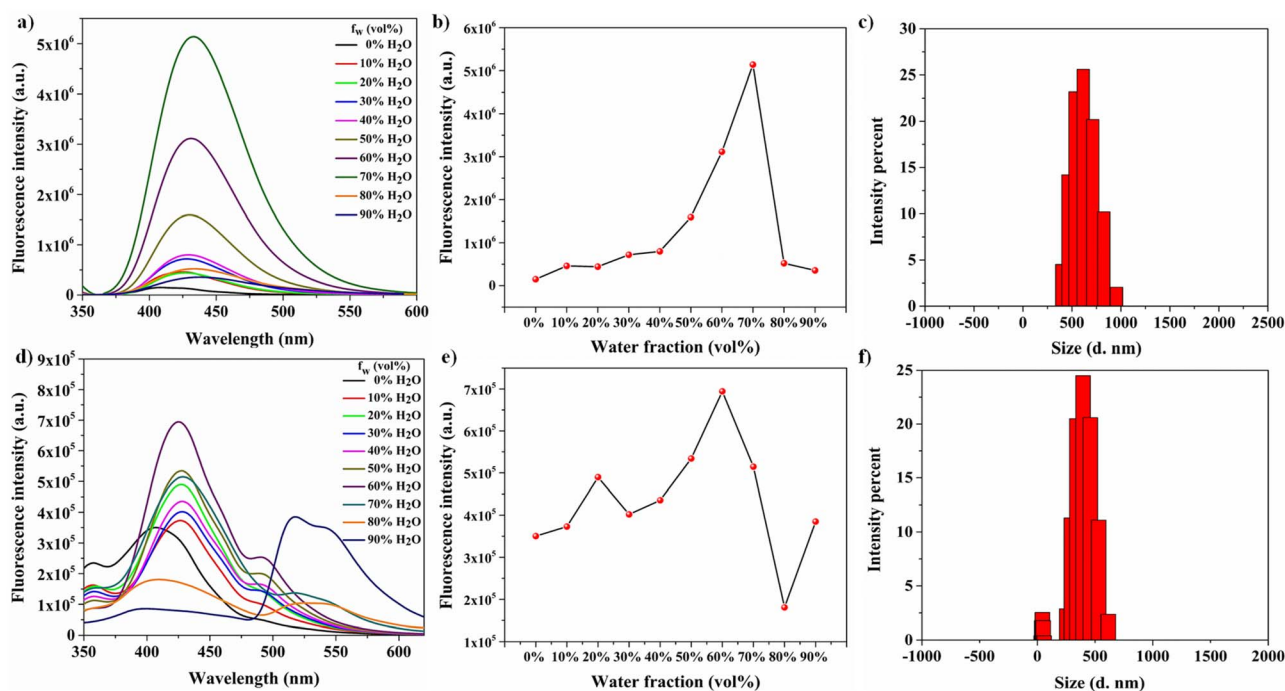
Fig. 4 (a) Emission spectra of **DBF1** (30 μM) in THF–water mixtures with varying water fractions (f_w); (b) Plot of emission intensity *versus* water percentages of **DBF1** in THF. λ_{ex} = 345 nm, concentration = 30 μM.; (c) DLS particle size distribution profile of **DBF1** in its aggregated state (70% water fraction); (d) emission spectra of **DBF2** (30 μM) in THF–water mixtures with varying water fractions (f_w); (e) plot of emission intensity *versus* water percentages of **DBF2** in THF. λ_{ex} = 324 nm, concentration = 30 μM.; (f) DLS particle size distribution profile of **DBF2** in its aggregated state (60% water fraction).

participation of an AIE phenomenon (Fig. 4b) behind the high emissive nature of **DBF1** in the aggregated and solid-state. In the case of **DBF2**, only a single peak at 409 nm was observed in THF solvent (0% water), suggesting an emission caused by the enol form of the molecule. As the water fractions increased, a red shift was observed in the emission spectra, and an increase in the emission intensity was also observed, with the highest intensity at 60% water fraction. As seen in Fig. 4d, **DBF2** showed high emission in THF solvent, which then enhanced as the water fraction increased, suggesting the involvement of the AIEE phenomenon (Fig. 4e). Moreover, a new peak emerged at longer wavelengths with a maximum at λ_{em} 518 nm, which can be attributed to the keto form of the molecule **DBF2**.[37] The aggregate formation was also verified from the DLS (dynamic light scattering) studies (Fig. 4c and f). The hydrodynamic diameter (Z-average in nm) for **DBF1** and **DBF2** was found to be 611.5 nm and 403.1 nm, respectively. The results obtained from the DLS particle size analysis and the emission spectra of varying water fractions show that **DBF1** and **DBF2** exhibited an ESIPT-AIE and ESIPT-AIEE phenomena, respectively, leading to high fluorescence intensity both in the solid and aggregated states. Other photophysical properties of both compounds, including the molar extinction coefficient and relative quantum yield, both in solution and aggregated states, were also investigated. The excitation maxima, emission maxima, particle size (hydrodynamic diameter), molar extinction coefficient, and relative fluorescence quantum yield (φ_f) were calculated and are tabulated in Table 1.
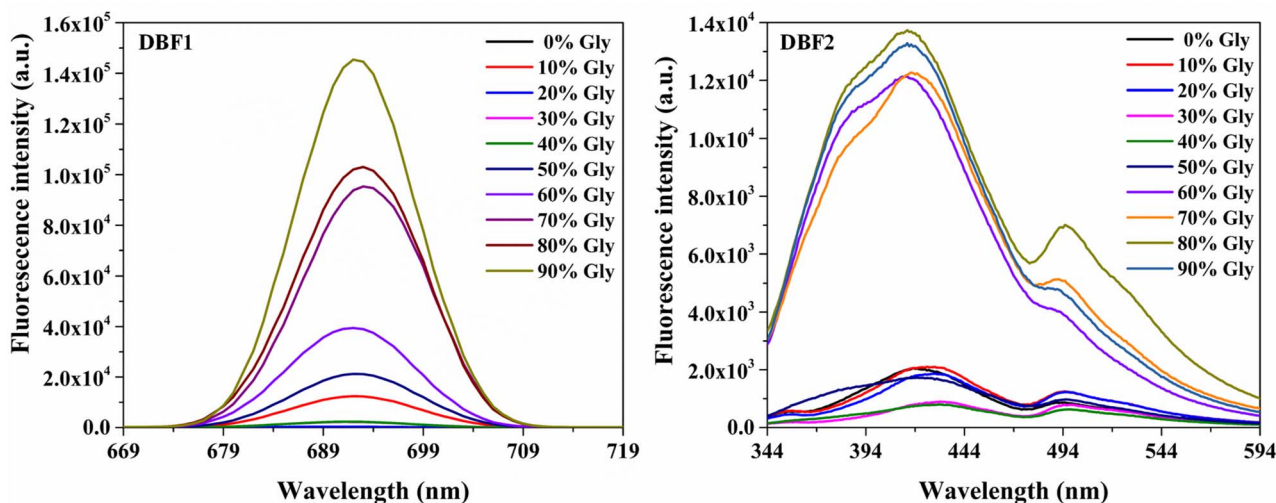
A viscofluorochromism study was conducted to investigate the impact of the viscosity of the medium on the emission profiles of both molecules. As shown in Fig. 5, both molecules were weakly emissive in THF, and upon consecutive addition of glycerol, the overall viscosity of the medium gradually increased, which restricts the molecular motions, resulting in the enhancement of the emission by the molecules. From Fig. 5, it can be seen that the emission efficiency increased as the viscosity of the medium increased. The results showed that the increased viscosity of the medium resulted in increased emission by the molecules, indicating the involvement of aggregation-induced emission.

The photostability of both molecules was also studied in solid-state (Fig. S12) by recording fluorescence spectra from 0 minutes to 60 minutes at an interval of 15 minutes each. A negligible decrease in the fluorescence intensity was found for both molecules, indicating the high fluorescence stability of the molecules. The molar extinction coefficient represents the fluorophore's ability to absorb light within a specific wavelength. A high molar extinction coefficient (MEC) value with a high fluorescence quantum yield value ensures better emission properties.[38] Therefore, it is important to develop fluorophores with high MEC to improve the quantity of absorbed photons, which further improves the emission properties of the molecules. Therefore, it is important to develop fluorophores with high MEC to improve the quantity of absorbed photons, which significantly improves the chances of better fluorescence properties for the fluorophores. We calculated the MECs for

Table 1 Photophysical properties of DBF1 and DBF2 in the aggregate state

Compound	$\lambda_{\text{max. abs.}}$ (nm) in aggregated state	λ_{em} (nm) in aggregated state	Z-avg. (d nm) in agg. State	Molar extinction coefficient ($\times 10^4$) L mol^{-1} cm^{-1}	Relative quantum yield (φ_f) %
DBF1	324	433	611.5	2.0	17.89
DBF2	321	424	403.1	0.69	2.26

Fig. 5 Viscofluorochromism of DBF1 [excitation wavelength = 345 nm] and DBF2 [excitation wavelength = 324 nm] in THF: glycerol (v/v) fractions (concentration used = 30 μM).

both compounds in their aggregate states using absorbance spectroscopy. For DBF1, the MEC obtained was 2.01×10^4 L mol^{-1} cm^{-1}, which was higher than that of DBF2, with a value of 0.69×10^4 L mol^{-1} cm^{-1}. These results indicated that the absorbance performance of DBF1 was much better than that of DBF2, which is consistent with the results obtained from emission properties in aggregate states and the quantum yield values obtained, as shown in Table 1. The relative quantum yield values were also calculated using a 30 μM solution of quinine sulfate in 1 M H$_2$SO$_4$. DBF1 exhibited a quantum yield of 17.89% in its aggregated state, 30 times more than its quantum yield of 0.58% in THF solution alone. In the case of DBF2, the compound also showed high emission in THF, with a relative quantum yield of 1.8%, which was then improved in its aggregated state to a value of 2.26%. A comparison of previously reported organic fluorophores for bioimaging with the molecules in this work is tabulated in Table 2, which indicates that the molecules DBF1 and DBF2 synthesized in this work exhibit better emissive properties than those of a few reported earlier. As mentioned before, a high molar extinction coefficient and quantum yield value lead to better emissive properties of the molecules. The results conclude that DBF1 has superior emissive properties to DBF2 in the aggregated state.

2.3 Cytotoxicity of DBF1 and DBF2 against HeLa cell lines

In order to explore the bioimaging potential of compounds DBF1 and DBF2, it is important to evaluate their toxicity. The *in vitro* cytotoxicity of these organic fluorophores against HeLa1 cell lines was evaluated using a standard MTT assay. The HeLa cells were treated with different concentrations of DBF1 and DBF2, *i.e.*, 10, 50, 100, 150, and 200 μg ml^{-1}, and were incubated for 24 hours (Fig. 6). Fig. 6a and c depict the %cell viability of HeLa cells at different concentrations of DBF1 and DBF2, respectively. Fig. 6b and d represent the microscopic observations of the compounds DBF1 and DBF2-treated HeLa cell lines, respectively. The standard control used for the study was camptothecin (20 μM). A table representing %cell viability and IC$_{50}$ values is tabulated in the SI (Tables S3 and S4). A chart of comparative IC$_{50}$ values of both compounds is depicted in Fig. 7. The MTT assay results suggest that compounds DBF1 and DBF2 showed effective toxicity towards HeLa cells with low IC$_{50}$ values of 42.08 μg ml^{-1} and 39.74 μg ml^{-1}, respectively, for 24 hours of treatment. From the results obtained, the significant toxic nature of fluorophores at lower concentrations, it is evident that these fluorophores exhibit potential anti-proliferative properties against HeLa cells.

2.4 Bioimaging of HeLa cell lines using DBF1 and DBF2

The prior results obtained indicate that both compounds possess good emissive properties in solid and aggregated states, demonstrating their candidacy for cell imaging applications. The applicability of the synthesized organic fluorophores as bioimaging probes was assessed using the confocal microscopy technique. HeLa cells were incubated with IC$_{50}$ concentrations,

Table 2 Comparison of previously reported fluorescent probes for bioimaging with the present work
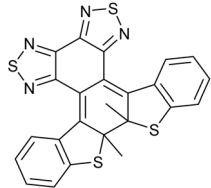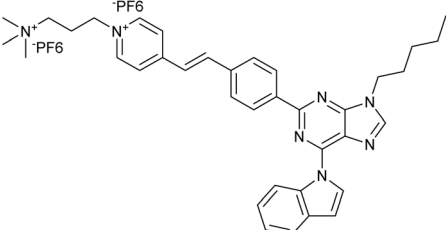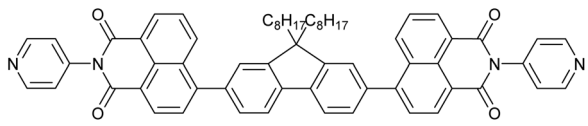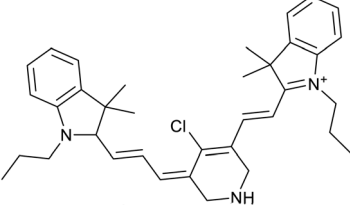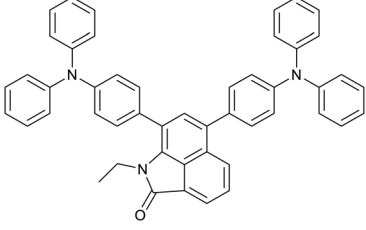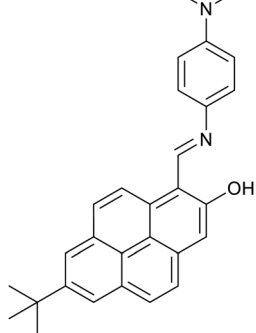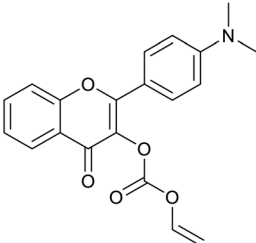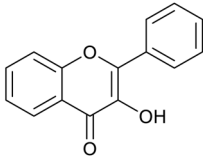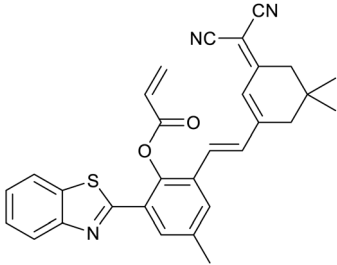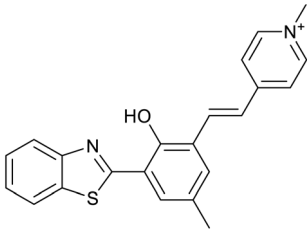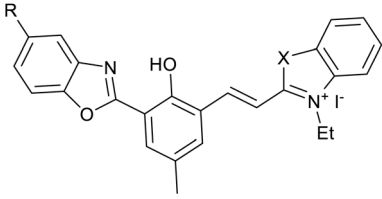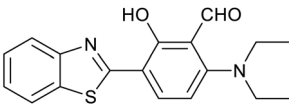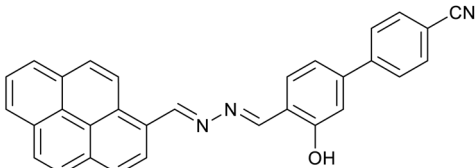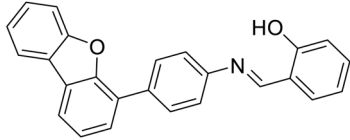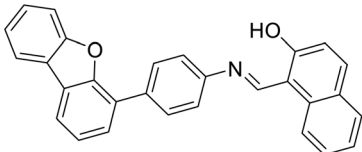
Sl. no.	Compound structure	Quantum yield in aggregate state (%)	Application	Ref.
1		7.22	Imaging	39
2		15.1	Bioimaging in HEK293, HepG2, HeLa, mouse cancer cell B16	40
3		0.4	Cell imaging in HeLa cells	41
4		3.16	Bioimaging in HeLa cells	42
5		0.92	Bioimaging in HUV cells	43
6		2.5%	Bioimaging in human fibroblasts and osteosarcoma cells	44
7		—	Two-photon ratiometric fluorescent probe for bioimaging of palladium species in HeLa cells	45

Table 2 (*Contd.*)

Sl. no.	Compound structure	Quantum yield in aggregate state (%)	Application	Ref.
8		0.039 with metal ions Ga(III): 0.791, Al(III): 1.027, In(III): 1.032	Fluorescent imaging of group IIIA ions in HeLa and A549 cells	46
9		—	Detection of cysteine and its bioimaging in HeLa cells and mice	47
10		0.06	Fluorescent probe for neuromasts in zebrafish	48
11	Probe 2 (R=H, X=S) Probe 3 (R=H, X=CMe₂)	Probe 2: 0.28 Probe 3: 0.27	Probe 2: fluorescent probe for lysosome Probe 3: fluorescent probe for mitochondria	49
12		0.69% in pH = 7 69% in pH = 2	pH sensor in MG-63 cells and *E. coli* bacteria	50
13		—	Cyanide detection in food, *C. elegans*, mice, and HeLa cells	51
14		2.26	Bioimaging in HeLa cells	**This work**
15		17.89	Bioimaging in HeLa cells	**This work**

Fig. 6 (a) %cell viability values of HeLa cells treated with varying concentrations of **DBF1** after the incubation period of 24 hours by MTT assay. (b) An overlaid montage photo represents the morphology of HeLa cells treated with different con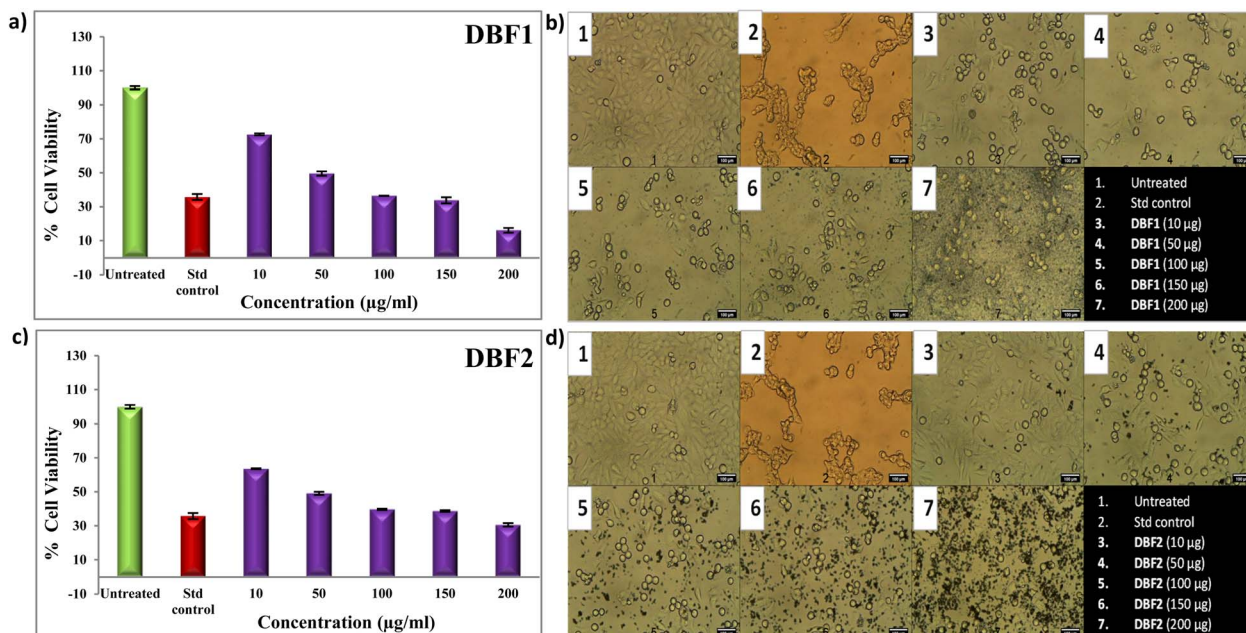centrations of **DBF1** after an incubation period of 24 hours. (c) %cell viability values of HeLa cells treated with varying concentrations of **DBF2** after the incubation period of 24 hours by MTT assay. (d) An overlaid montage photo represented the morphology of HeLa cells treated with different concentrations of **DBF1** after an incubation period of 24 hours.
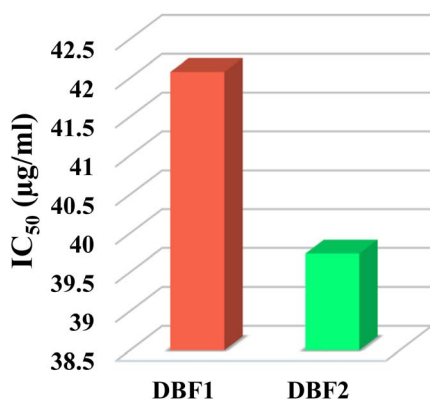

Fig. 7 Comparison chart of IC_{50} values of **DBF1** and **DBF2** against the HeLa cells after the incubation period of 24 hours by MTT assay.

i.e., 42.08 µg ml^{-1} and 39.74 µg ml^{-1}, of **DBF1** and **DBF2**, respectively, for 6 hours. After incubation, the cells were observed under a Carl Zeiss LSM 880 Fluorescence Live cell imaging system (Confocal Microscope) with filter cubes of DAPI, FL1, and Bright field (Fig. 8). Fig. 9 depicts the cellular uptake studies by confocal microscopy, suggesting that the given molecules showed good fluorescence intensity values in HeLa cells after 6 hours of incubation. These results confirmed the significant cellular uptake effect at 6 hours by penetrating inside the cell membrane and the ability to fluoresce in cellular conditions. Compared to the untreated cells, which showed a very low intensity of mean fluorescence intensity signal with a value of 0.048 ± 0.01 a.u., **DBF1** and **DBF2** exhibited

exceptional fluorescence intensities with a relative mean fluorescence intensity of 1.008 ± 0.77 a.u. and 1.44 ± 0.65 a.u., respectively (Fig. 8b).

2.5 Synthesis

To develop ESIPT-based fluorophores, having an *ortho* hydroxy group adjacent to an imine (–C=N) moiety is very important.[52] Considering the general ESIPT-active molecular structure, we designed molecules **DBF1** and **DBF2** with salicylaldehyde and 2-hydroxy-1-naphthaldehyde, respectively. As shown in Scheme 1, **DBF1** and **DBF2** were prepared by a simple Schiff base reaction between 4-(dibenzo[*b,d*]furan-4-yl)aniline and salicylaldehyde and 2-hydroxy-1-naphthaldehyde, respectively. The products obtained were characterized using ^{1}H NMR, ^{13}C NMR spectra, LC-MS, and FTIR (Fig. S1–S8).

3 Experimental section

3.1 Materials and methods

All the starting materials were purchased from commercial chemical suppliers and used without further purification. 4-(dibenzo[*b,d*]furan-4-yl)aniline, 2-hydroxybenzaldehyde, and 2-hydroxy-1-naphthaldehyde were procured from BLD, Avra, and Merck and were utilized without further purification. All the solvents used were purchased from Thomas Baker, Spectrochem, SDFCL, and Avra and were used without further purification. HPLC grade solvents were used for the UV-visible and fluorescence spectroscopy studies and were obtained from Spectrochem. The reactions were monitored *via* thin layer
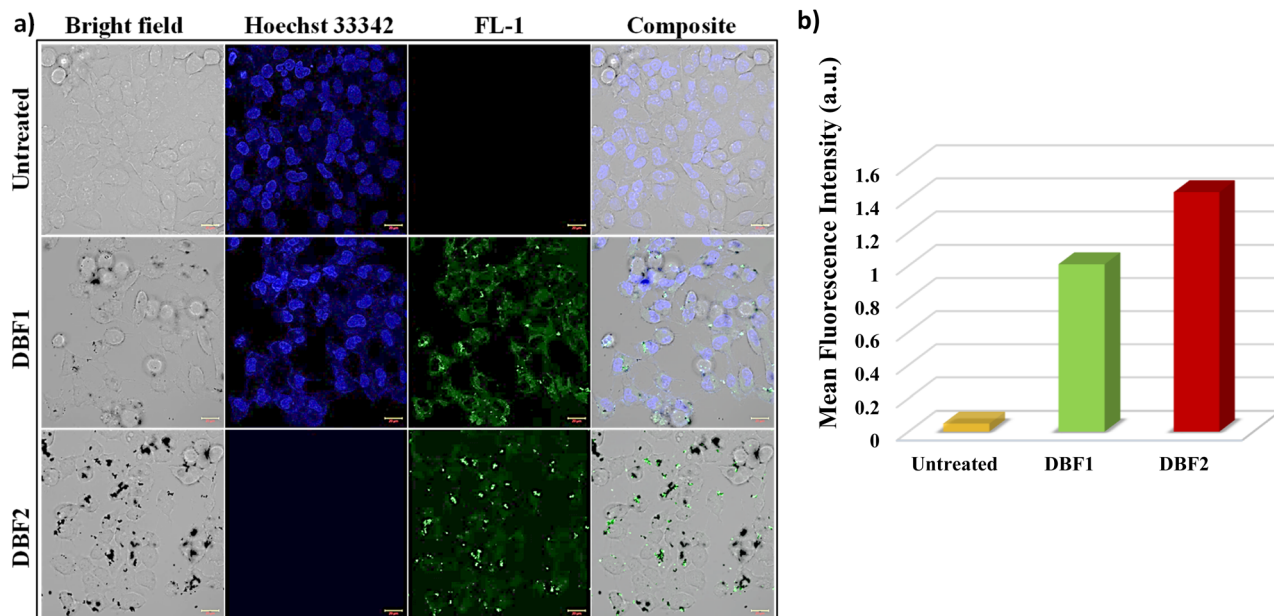
Fig. 8 (a) Confocal microscopy images of HeLa cells treated with 42.08 μg ml^{-1} and 39.74 μg ml^{-1} of **DBF1** and **DBF2**, respectively, for 6 hours of incubation (excited with a 488 nm laser, and the emission was collected with the 522 nm filter). (b) A plot of comparison of the mean fluorescence intensity of **DBF1** and **DBF2** in confocal images in HeLa cell lines.
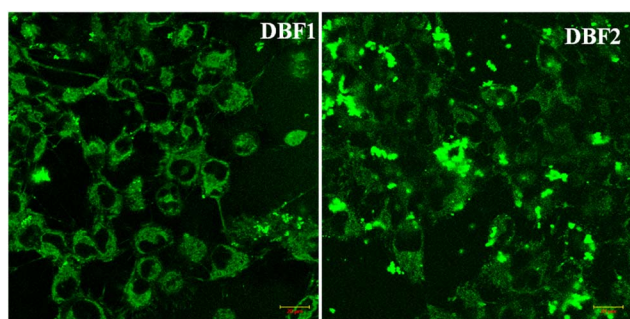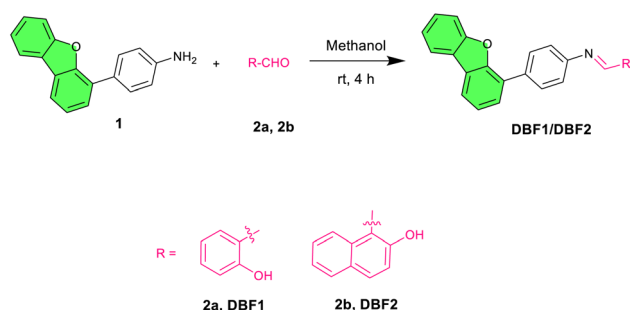

Fig. 9 Cell imaging of HeLa cell lines after 6 h of incubation with **DBF1** and **DBF2** under a fluorescent microscope, green channel.

Scheme 1 One-pot synthesis route towards dibenzo[b,d]furan-based fluorophores **DBF1** and **DBF2**.

chromatography using pre-coated silica gel 60 F254 plates (Merck & Co.) and observed using a 365 nm UV lamp. The NMR spectra were recorded at room temperature (~28 °C) in DMSO-d_6 on a Bruker Avance 400 MHz. For ^{1}H NMR, tetramethylsilane (TMS) was the internal standard. The spectra data presented here are reported as follows: chemical shift, integration, multiplicity (s = singlet, d = doublet, t = triplet, q = quartet, m = multiplet), and coupling constant (s) in Hertz. For ^{13}C NMR, TMS ($\delta = 0$) was used as the internal standard, and spectra were obtained with complete proton decoupling. LC-MS was obtained using an ESI ionization using the LCMS-8060NX instrument from Shimadzu. Melting point tests were carried out on an electrothermal melt-temperature apparatus. Infrared spectra were recorded using a Bruker Tensor 27 FT-IR spectrophotometer, UV-visible spectra were recorded on a SHIMADZU UV-1800, and fluorescence spectra were recorded on the FluoroMax® Plus by HORIBA Scientific. The dynamic light scattering (DLS) studies were carried out using a MALVERN Zetasizer Nano ZS instrument (ZEN 3600). Laser confocal scanning microscope images were collected on a Confocal fluorescence Microscope with a live cell imaging system (Carl Zeiss LSM 880, Germany). The absorbance for MTT analysis was recorded on xMark Microplate Absorbance spectrophotometer (1681150, BioRad, CA, USA) at a wavelength of 570 nm. Images were analyzed using ZEN Blue software, and the relative fluorescence intensity values of FITC were measured using Image J (FIJI) Software.

3.2 Photophysical studies

The photophysical studies, including the studies conducted for aggregation-induced emission, were conducted with a 30 μM solution in THF.

3.3 Cell culture

The cell line studies were conducted at Averin Biotech Labs, Bangalore, India. HeLa cells were procured from the National Centre for Cell Sciences, Pune, India. The cells were maintained

in DMEM with high glucose media supplemented with 10% FBS along with the 1% antibiotic–antimycotic solution in an atmosphere of 5% CO_2, 18–20% O_2 at 37 °C temperature in the CO_2 incubator and sub-cultured every 3 days.

3.4 Cytotoxicity-MTT assay

All cells were seeded into 96-well plates at a density of 20 000 cells per well and allowed to grow for about 24 hours. The cells were treated with appropriate concentrations of both synthesized dibenzofuran-based molecules. The plates were incubated for 24 hours at 37 °C in a 5% CO_2 atmosphere. After the incubation period, the plates were taken out; the spent was removed, and freshly prepared 3-(4,5-dimethylthiazol-2-yl) 2,5-diphenyl tetrazolium bromide (MTT) reagent (0.5 mg ml^{-1} of total volume) was added. The plates were wrapped with aluminum foil to avoid exposure to light. The 96-well plate was incubated at 37 °C for 3 hours. After 3 hours, the MTT reagent was removed, and 100 µl of solubilization solution (DMSO) was added. The cell wells were kept in a gyratory shaker to dissolve MTT formazan crystals. The absorbance was recorded on xMark Microplate Absorbance spectrophotometer (1681150, BioRad, CA, USA) at a wavelength of 570 nm. %Cell viability is calculated using the following formula:

$$\%\text{Cell viability} = [\text{mean abs of treated cells/mean abs of untreated cells}] \times 100$$

The IC_{50} value was determined using a linear regression equation, i.e., $Y = M_x + C$ ($Y = 50$, M and C values were derived from the viability graph). The anticancer activities of the synthesized dibenzofuran-based fluorophores were evaluated against HeLa cells (Human cervix adenocarcinoma cell lines). Camptothecin, a commercial anti-cancer drug effective against DNA topoisomerase type II, was used as a standard control.

3.5 Cellular uptake (bioimaging)

HeLa cells were seeded in a 35 mm glass-bottom dish at 0.5×10^5 cells per 1 ml density in 1 ml of DMEM with high glucose medium (cat no: 11965-084, Gibco)and incubated in a CO_2 incubator overnight at 37 °C for 24 hours. The spent medium was aspirated, and the cells were treated with the synthesized organic fluorophores using their IC_{50} concentrations for 6 hours without exposure to light. After the treatment, the medium was removed from all the wells and washed with sterile PBS. The cells were counter-stained with 5 µg ml^{-1} of Hoechst 33342 solution. The cells were observed and recorded by Carl Zeiss LSM 880 Fluorescence Live cell imaging system (Confocal Microscope) with DAPI, FL1, and bright-field filter cubes. Images were analysed using ZEN Blue software, and the relative fluorescence intensity values of FITC were measured using Image J (FIJI) Software.

3.6 Synthesis procedures

3.6.1 Synthesis of (E)-2-((4-(dibenzo[b,d]furan-4-yl) phenylimino)methyl)phenol (DBF1). To a solution of 4-(dibenzo[b,d]furan-4-yl)aniline (1.6 mmol, 1 equiv., 424.66 mg) in methanol taken in an over-dry 50 ml round-bottom flask, 2-hydroxybenzaldehyde (1.6 mmol, 1 equiv., 200 mg) was added. The reaction mixture was stirred at room temperature for 4 hours. The reaction was monitored using thin-layer chromatography (TLC). The completion of the reaction was confirmed by observing the formation of a yellow fluorescent spot at $R_f = 0.6$ in 15% ethyl acetate: hexanes. After the reaction, the pale yellow solid formed was filtered off and washed with methanol. A complete conversion of the starting materials was observed. The crude product was purified by several washes with hot methanol. Column purification was done using silica gel (100–200 mesh) with 5% EtOAc in hexanes (v/v) to yield a yellow-coloured product in high yields of 98.63%.

DBF1. $C_{18}H_{13}NO_2$; yield: 587 mg, 98.63%; IR (cm^{-1}): 3040, 2916, 2854, 1615, 1565, 1487, 1448, 1388, 1361, 1281, 1180, 1064, 1014, 973, 910, 842, 793, 742, 666, 561. Melting point: 111–115 °C. NMR spectroscopy: ^1H NMR (400 MHz, DMSO-d_6, 28 °C, δ): 13.11 (s, 1H), 9.08 (s, 1H), 8.23–8.17 (m, 3H), 8.05–8.03 (m, 2H, doublets signals are merged), 7.77 (d, $J = 8$ Hz, 2H), 7.72 (d, $J = 6.8$ Hz, 1H), 7.64–7.62 (m, 2H, doublets signals are merged), 7.58–7.52 (m, 2H), 7.45 (t, $J = 7.6$ Hz, 2H), 7.04–6.99 (m, 2H). ^{13}C NMR (101 MHz, DMSO-d_6, 28 °C, δ): 164.16, 160.81, 155.92, 153.00, 148.17, 134.69, 133.91, 133.10, 130.03, 128.27, 127.24, 124.94, 124.83, 124.26, 123.96, 123.76, 122.36, 121.75, 120.96, 119.87, 119.70, 117.13, 112.29. Mass spectrometry: LCMS (ESI) m/z: calcd. for $C_{18}H_{13}NO_2$; actual = 363.10, found = 364.

3.6.2 Synthesis of (E)-1-(((4-(dibenzo[b,d]furan-4-yl)phenyl)imino)methyl)naphthalen-2-ol (DBF2). A solution of 4-(dibenzo[b,d]furan-4-yl)aniline (1.162 mmol, 1 equiv., 301 mg) in methanol was taken in a hot air oven-dried 50 ml round-bottom flask. To this, 2-hydroxy-1-naphthaldehyde (1.162 mmol, 1 equiv., 200 mg). The reaction mixture was then stirred at room temperature for 4 hours. The completion of the reaction was monitored with thin-layer chromatography (TLC). The completion of the reaction was confirmed by observing the formation of a yellow fluorescent spot at $R_f = 0.65$ in 15% ethyl acetate: hexanes. After the reaction, the yellow solid formed was filtered off and washed with methanol. The crude product was washed with hot methanol. Column purification was performed using silica gel (100–200 mesh) with 5% EtOAc in hexanes (v/v) to yield an orange-coloured product in high yields of 96.88%.

DBF2. $C_{29}H_{19}NO_2$; yield: 465 mg, 96.88%; IR (cm^{-1}): 3721, 3046, 2979, 1615, 1564, 1515, 1484, 1450, 1391, 1323, 1174, 1089, 1009, 962, 830, 787, 739, 595. Melting point: 227–232 °C. NMR spectroscopy: ^1H NMR (400 MHz, DMSO-d_6, 28 °C, δ): 15.82 (s, 1H), 9.74 (s, 1H), 8.53 (d, $J = 8.4$ Hz, 1H), 8.29–8.16 (m, 2H), 8.07–8.05 (m, 2H, doublet signals have merged), 7.95 (d, $J = 9.2$ Hz, 1H), 7.85–7.81 (m, 3H), 7.79–7.75 (m, 2H), 7.58–7.52 (m, 3H), 7.45 (t, $J = 7.2$ Hz, 1H), 7.37 (t, $J = 7.6$ Hz, 1H), 7.02 (d, $J = 9.2$ Hz, 1H). ^{13}C NMR (101 MHz, DMSO-d_6, 28 °C, δ): 164.16, 160.81, 155.92, 153.00, 148.17, 134.69, 133.91, 133.10, 130.03, 128.27, 127.24, 124.94, 124.83, 124.26, 123.96, 123.76, 122.36, 121.75, 120.96, 119.87, 119.70, 117.13, 112.29. Mass

spectrometry: LCMS (ESI) m/z: calcd. for $C_{29}H_{19}NO_2$, actual = 413.14, found = 413.

4 Conclusions

In this work, the properties of two novel dibenzo[b,d]furan-based fluorophores, **DBF1** and **DBF2**, were systematically evaluated for their bioimaging applications in HeLa cell lines. Within the scope of our research, this is the first report of dibenzo[b,d]furan-based fluorophores for bioimaging applications. The photophysical properties of both the fluorophores were investigated in both solution and aggregated states, indicating the involvement of AIE and AIEE properties. The molar extinction coefficients for **DBF1** and **DBF2** were found to be 2.0×10^4 L mol^{-1} cm^{-1} and 0.69×10^4 L mol^{-1} cm^{-1}, respectively, in their aggregate state, showcasing exceptional absorption properties. The synthesized fluorophores **DBF1** and **DBF2** exhibited superior emissive properties, with relative fluorescence quantum yields of 17.8% and 2.26%, respectively. Both fluorophores showed notable fluorescence intensity in HeLa cell lines with relative mean fluorescence intensity values of 1.008 ± 0.77 a.u. and 1.44 ± 0.65 a.u., respectively. Moreover, the large Stokes shift of ESIPT and the signal amplification of AIE gave the fluorophores a high signal-to-noise ratio. Owing to their excellent emission properties in solid, aggregated states and in cell lines, **DBF1** and **DBF2** act as promising candidates for imaging in biological environments. Thus, the key attributes such as high emissive nature, superior quantum yields, and high molar extinction coefficients of this new class of compounds highlight their significance in image-guided surgery.

Author contributions

Nikita Kush Durgi: conceptualization, methodology, investigation, visualization, writing – original draft, writing – review & editing. Prasad Pralhad Pujar: supervision, funding acquisition, writing – review & editing.

Conflicts of interest

There are no conflicts to declare.

Data availability

All data are available in the manuscript and SI. Supplementary information is available. See DOI: https://doi.org/10.1039/d5ra05626h.

Acknowledgements

References

1 K. Li, T.-B. Ren, S. Huan, L. Yuan and X.-B. Zhang, *J. Am. Chem. Soc.*, 2021, **143**, 21143–21160.

2 H. Kobayashi, M. Ogawa, R. Alford, P. L. Choyke and Y. Urano, *Chem. Rev.*, 2010, **110**, 2620–2640.

3 J. Chan, S. C. Dodani and C. J. Chang, *Nat. Chem.*, 2012, **4**, 973–984.

4 D. Wu, A. C. Sedgwick, T. Gunnlaugsson, E. U. Akkaya, J. Yoon and T. D. James, *Chem. Soc. Rev.*, 2017, **46**, 7105–7123.

5 S. Gao, D. Chen, Q. Li, J. Ye, H. Jiang, C. Amatore and X. Wang, *Sci. Rep.*, 2014, **4**, 4384.

6 L. Bu, B. Shen and Z. Cheng, *Adv. Drug Delivery Rev.*, 2014, **76**, 21–38.

7 A. S. Klymchenko, *Acc. Chem. Res.*, 2017, **50**, 366–375.

8 S. Thangudu, P. Kalluru and R. Vankayala, *Bioengineering*, 2021, DOI: **10.1039/D1BM00631B**.

9 F. Duan, M. Hu, C. Guo, Y. Song, M. Wang, L. He, Z. Zhang, R. Pettinari and L. Zhou, *Chem. Eng. J.*, 2020, **398**, 125452.

10 S. Xu, H.-W. Liu, S.-Y. Huan, L. Yuan and X.-B. Zhang, *Mater. Chem. Front.*, 2021, **5**, 1076–1089.

11 H.-B. Cheng, Y. Li, B. Z. Tang and J. Yoon, *Chem. Soc. Rev.*, 2020, **49**, 21–31.

12 M. Wang, G. Zhang, D. Zhang, D. Zhu and B. Z. Tang, *J. Mater. Chem.*, 2010, **20**, 1858.

13 H. Li, Q. Yao, W. Sun, K. Shao, Y. Lu, J. Chung, D. Kim, J. Fan, S. Long, J. Du, Y. Li, J. Wang, J. Yoon and X. Peng, *J. Am. Chem. Soc.*, 2020, **142**, 6381–6389.

14 F. Zhang and B. Z. Tang, *Chem. Sci.*, 2021, **12**, 3377–3378.

15 K. Y. Zhang, Q. Yu, H. Wei, S. Liu, Q. Zhao and W. Huang, *Chem. Rev.*, 2018, **118**, 1770–1839.

16 J. E. Kwon and S. Y. Park, *Adv. Mater.*, 2011, **23**, 3615–3642.

17 J. Zhao, S. Ji, Y. Chen, H. Guo and P. Yang, *Phys. Chem. Chem. Phys.*, 2012, **14**, 8803–8817.

18 A. Douhal, F. Lahmani and A. H. Zewail, *Chem. Phys.*, 1996, **207**, 477–498.

19 S. Lochbrunner, M. Thomas Schultz, J. P. Schmitt, M. Z. Shaffer and A. Zgierski, *J. Chem. Phys.*, 2001, **114**, 2519–2522.

20 Z. Tu, M. Liu, Y. Qian, G. Yang, M. Cai, L. Wang and W. Huang, *RSC Adv.*, 2015, **5**, 7789–7793.

21 Y. Li, D. Dahal, C. S. Abeywickrama and Y. Pang, *ACS Omega*, 2021, **6**, 6547–6553.

22 A. C. Sedgwick, L. Wu, H.-H. Han, S. D. Bull, X.-P. He, T. D. James, J. L. Sessler, B. Z. Tang, H. Tian and J. Yoon, *Chem. Soc. Rev.*, 2018, **47**, 8842–8880.

23 P.-Y. Fu, S.-Z. Yi, M. Pan and C.-Y. Su, *Acc. Mater. Res.*, 2023, **4**, 939–952.

24 H. Böhnke, J. Bahrenburg, X. Ma, K. Röttger, C. Näther, M. F. Rode, A. L. Sobolewski and F. Temps, *Phys. Chem. Chem. Phys.*, 2018, **20**, 2646–2655.

25 L. Peng, L. Xiao, Y. Ding, Y. Xiang and A. Tong, *J. Mater. Chem. B*, 2018, **6**, 3922–3926.

26 P. Zhou and K. Han, *Aggregate*, 2022, **3**(5), e160.

27 Y. Liu, B. Feng, X. Cao, G. Tang, H. Liu, F. Chen, M. Liu, Q. Chen, K. Yuan, Y. Gu, X. Feng and W. Zeng, *Analyst*, 2019, **144**, 5136–5142.

28 R. Banerjee, H. K. S. Kumar and M. Banerjee, *Int. J. Rev. Life Sci.*, 2012, **2**, 7–16.

29 P. Patel, R. Shakya, Vishakha, V. Asati, B. D. Kurmi, S. K. Verma, G. D. Gupta and H. Rajak, *J. Mol. Struct.*, 2023, 137098.

30 A. A. Abbas and K. M. Dawood, *RSC Adv.*, 2023, **13**, 11096–11120.

31 J. E. Kwon and S. Y. Park, *Adv. Mater.*, 2011, **23**(32), 3615–3642.

32 J. Cheng, D. Liu, W. Li, L. Bao and K. Han, *J. Phys. Chem. C*, 2015, **119**, 4242–4251.

33 X. Liu, A. Li, W. Xu, Z. Ma and X. Jia, *Mater. Chem. Front.*, 2019, **3**, 620–625.

34 Y. Wang, I. Zhang, B. Yu, X. Fang, X. Su, Y.-M. Zhang, T. Zhang, B. Yang, M. Li and S. X.-A. Zhang, *J. Mater. Chem. C*, 2015, **3**, 12328–12334.

35 S. Chen, W. Wang, M. Yan, Q. Tu, S.-W. Chen, T. Li, M.-S. Yuan and J. Wang, *Sens. Actuators, B*, 2018, **255**, 2086–2094.

36 P. Yadav, A. K. Singh, C. Upadhyay and V. P. Singh, *Dyes Pigm.*, 2019, **160**, 731–739.

37 M. A. Rauf, S. Hisaindee and N. Saleh, *RSC Adv.*, 2015, **5**, 18097–18110.

38 L. D. Lavis and R. T. Raines, *ACS Chem. Biol.*, 2008, **3**, 142–155.

39 H. Yang, M. Li, C. Li, Q. Luo, M.-Q. Zhu, H. Tian and W.-H. Zhu, *Angew Chem. Int. Ed. Engl.*, 2020, **59**, 8560–8570.

40 L. Shi, Y.-H. Liu, K. Li, A. Sharma, K.-K. Yu, M. S. Ji, L.-L. Li, Q. Zhou, H. Zhang, J. S. Kim and X.-Q. Yu, *Angew Chem. Int. Ed. Engl.*, 2020, **59**, 9962–9966.

41 Y. Zhang, Y. Qu, J. Wu, Y. Rui, Y. Gao and Y. Wu, *Dyes Pigm.*, 2020, **179**, 108431.

42 X. Ma, C. Zhang, L. Feng, S. H. Liu, Y. Tan and J. Yin, *J. Mater. Chem. B*, 2020, **8**, 9906–9912.

43 F. Yu, H. Zhao, Y. Li, G. Xia and H. Wang, *Mater. Chem. Front.*, 2022, **6**, 155–162.

44 Z. Chen, Y. Wang, X. Song, J. Zhang, Y. Zhang, S. Chen, Y. Cai, J. Li, M. R. J. Elsegood, X. Feng and J. He, *Dyes Pigm.*, 2026, **244**, 113111.

45 W. Luo, J. Li and W. Liu, *Org. Biomol. Chem.*, 2017, **15**, 5846–5850.

46 X. He, W. Xiong, L. Zhang, C. Xu, J. Fan, Y. Qian, J. Wen, F. Ding and J. Shen, *Dyes Pigm.*, 2020, **174**, 108059.

47 H. Ren, F. Huo, Y. Zhang, S. Zhao and C. Yin, *Sens. Actuators, B*, 2020, **319**, 128248.

48 L. McDonald, D. Dahal, M. Konopka, Q. Liu and Y. Pang, *Bioorg. Chem.*, 2019, **89**, 103040.

49 D. Dahal, S. Pokhrel, L. McDonald, K. Bertman, S. Paruchuri, M. Konopka and Y. Pang, *ACS Appl. Bio Mater.*, 2019, **2**, 4037–4043.

50 N. Singla, M. Ahmad, S. Dhiman, G. Kumar, S. Singh, S. Verma, S. Kaur, M. Rashid, S. Kaur, V. Luxami, P. Singh and S. Kumar, *New J. Chem.*, 2021, **45**, 19145–19153.

51 C. Bai, J. Zhang, Y. Qin, H. Huang, Z. Xia, Q. Zheng, H. Dai, P. Lu, H. Miao, C. Qu and R. Qiao, *Chem. Eng. J.*, 2022, **443**, 136445.

52 J. Wang, Q. Meng, Y. Yang, S. Zhong, R. Zhang, Y. Fang, Y. Gao and X. Cui, *ACS Sens.*, 2022, **7**, 2521–2536.